



Laser Cladding Novel NiCrSiFeBW–CeO₂ Coating with Both High Wear and Corrosion Resistance

Min Guo^{1,2,3} · Suiyuan Chen^{1,2,3} · Fanmin Shang^{1,2,3} · Jing Liang^{1,2,3} · Tong Cui^{1,2,3} · Changsheng Liu^{1,2,3} · Mei Wang⁴

Received: 6 March 2020 / Accepted: 28 April 2020 / Published online: 11 June 2020
© The Korean Institute of Metals and Materials 2020

Abstract

In order to obtain the high wear- and corrosion-resistant nickel based alloy coatings for laser remanufacturing fretting damaged metal parts which are serviced under high-temperature corrosion and wear conditions, a novel NiCrSiFeBW–CeO₂ alloy powder was designed by increasing the content of B and Si, adding tungsten and CeO₂ using JMatpro software on the basis of Ni60 alloy powder composition, and the NiCrSiFeBW–CeO₂ coating was successfully cladded on 45# steel under different laser energy area densities. The microstructure, wear and corrosion behaviors of the NiCrSiFeBW–CeO₂ coatings were systematically studied. The results show that novel NiCrSiFeBW–CeO₂ coating produced by laser cladding not only has no cracks but also has both high wear resistance and corrosion resistance due to some ultra-fine compound particle phases in situ generated in its structure. Among these phases, the B₃Cr₅, CrB₄, (Cr, Ni)₃C₂, Cr₇C₃, W₃Cr₁₂Si₅ and (Fe, Ni)₅Si₃ played a significant role in reinforcing the wear resistance of the coating, while the B₃Cr₅, W₃Cr₁₂Si₅ and CrB₄ enhanced the corrosion resistance of the coating. The novel NiCrSiFeBW–CeO₂ coating prepared under 100 J/mm² EAD has the best comprehensive performance, the wear loss is 7.53×10^{-5} mm³/N, the E_{corr} is – 0.1738 V. Compared with Ni60 alloy coating, the novel Ni-based coating not only has a better laser cladded formability but also similar wear resistance and better corrosion-resistance. It provides a reference for repairing fretting damaged metal parts by laser cladding the nickel based coating with high wear and corrosion resistance.

Keywords Laser remanufacturing · Fretting damaged metal part · Ni-based coating · In-situ generated phase · Wear resistance · Corrosion resistance

1 Introduction

When a mechanical part is serviced under high-temperature wear and corrosion conditions, fretting behavior usually occurs, which could cause equipment damage and lead to the waste of resources during repairing, especially for short

stress wire mills. Laser remanufacturing technology is one of the emerging repair and remanufacturing technologies [1–3], which is often be used to repair the surface of damaged parts by cladding the wear- and corrosion-resistant coatings to obtain a better comprehensive performance [4, 5]. Besides, due to the complex served conditions of the key parts of the rolling mill (550–700 °C, high level Cl[–] ions concentration), only the alloy coatings with both high wear resistance and corrosion resistance can meet repair requirement. Ni-based coating has been widely used for laser repair and remanufacturing of failed parts under various corrosive and wear conditions due to its good corrosion resistance and wear resistance. Among them, the high hardness Ni60 alloy coating is widely used in the repair of wear-out parts, but it is easy to crack during laser cladding process, and the corrosion resistance of the coating can't meet the repairing requirements for high-temperature corrosion and wear conditions. Actually, the wear- and corrosion-resistant of the currently existing Ni-based powder and coatings can not satisfy the

✉ Suiyuan Chen
chensy@atm.neu.edu.cn

¹ Key Laboratory for Anisotropy and Texture of Materials, Ministry of Education, Northeastern University, Shenyang 110819, China
² Key Laboratory for Laser Application Technology and Equipment of Liaoning Province, Northeastern University, Shenyang 110819, China
³ School of Materials and Engineering, Northeastern University, Shenyang 110819, China
⁴ Ministry of Science and Technology, Shenyang Dalu Laser Technology Co. Ltd., Shenyang 11000, China

repair requirements of the failed components. Therefore, the design of laser cladding remanufacturing of novel Ni-based powder with both wear resistance and corrosion resistance to meet fretting damage has become a novel research topic.

So far, many researches have focused on laser cladding Ni-based coatings for laser remanufacturing. In terms of wear resistance research, Weng et al. [6] studied the effect of different WC particles content on the wear resistance of Ni/WC (0–60 wt%) composite coating, and found that the increase of WC content could significantly improve the wear resistance of the coating. Zhou et al. [7] added 35% WC particles to Ni60 alloy powder, and prepared Ni60 + WC composite coatings with high microhardness, no cracks and porosity defects by LIHRC method. Sun et al. [8] enhanced the wear resistance of Ni-based coatings by in situ titanium-doped NbC composite particles. Liu et al. [9] prepared NiCr–Cr₃C₂/30 wt%WS₂ and NiCr–Cr₃C₂/30 wt%WS₂ (Ni–P) self-lubricating wear-resistant composite coatings with no cracks and no pores by adding the WS₂ powder and the WS₂ coated with a layer of micro Ni–P powder worked as solid lubricant to NiCr–Cr₃C₂ powder. Luo et al. [10] revealed the effect of microstructure and hardness change of WC + Ni–NiCrBSi composite coating on wear behavior. Chen et al. [11] reported that the proper scanning speed in continuous local induction cladding technology can make NiCrBSi coatings obtain good wear performance.

In terms of corrosion resistance research, Wang et al. [12] added different contents of CeO₂ to improve the corrosion resistance of Ni60 alloy coating, founding that the corrosion resistance of 4 wt% CeO₂ + Ni60 alloy composite coating was 1.43 times than that of Ni60 alloy coating. He et al. [13] prepared the Al–Ni–TiC–CeO₂ composite coating with good corrosion resistance on S355 marine steel by laser cladding. They found that TiC particles in coatings improved the corrosion resistance and wear resistance. Zhang et al. [14] studied the corrosion resistance features of TiC-reinforced Inconel 718 composite coating prepared by SLM on different cross-sections, and found that the YZ plane with a thinner column had higher corrosion performance.

Although the wear resistance of the coating can be significantly improved by directly adding the hard ceramic particle in the alloy powder, the thermal expansion coefficient between the ceramic phase and the metal matrix is quite different. The addition of too much hard phase will lead to the cracking of the coating and reduce its the corrosion resistance [15]. At present, many scholars have been conducting researches on highly wear- or corrosion-resistant

Ni-based coatings, and some of them are compelling, but most reports focus on a single property (corrosion resistance or wear resistance). As we know, Ni60 alloy powder is a key powder to produce wear resistant coating by laser cladding, but it can hardly meet the requirements for repairing the parts after extensive corrosion and wear due to its poor laser formability. In this work, based on our previous researches, a novel Ni-based self-fluxing powder with both wear- and corrosion-resistant and better laser cladded formability was designed by JMatpro calculation on the basis of Ni60 alloy powder composition system. With the augment of B and Si elements content, the melting point of the coating can be reduced, the temperature zone of solid–liquid phase line can be enlarged, and low melting eutectic with Ni, Cr and W alloy elements can be formed to further harden and strengthen the coating. The added rare earth oxide (such as CeO₂, Y₂O₃ etc.) could refine γ -Ni type phase grain, strengthen γ -Ni type phase boundary and improve the properties of Ni-based coating [16–18]. Besides, the effects of microstructure and wear- and corrosion-resistant features of the NiCrSiFeBW–CeO₂ coating prepared under different laser energy area density (EAD) were systematically studied. The results of this paper might provide a reference for laser remanufacturing parts of short stress wire mill.

2 Materials and Methods

2.1 Materials

The main chemical components of Ni60 alloy powder (C1) and the NiCrSiFeBW–CeO₂ powder (C2) are presented in Table 1. 45# steel with dimensions of 180 mm × 100 mm × 10 mm was selected as the substrate. The C1 and C2 coating simulation under the equilibrium solidification condition were carried out in the nickel base alloy module of JMatpro software, in which the element content value of the simulated C1 and C2 alloy is directly input in this module (i.e. the content of various elements in C1 and C2 alloy in Table 1), and then the temperature–phase (T–P) diagram of these alloys were obtained in the thermodynamics plate. Before laser cladding process, 45# steel plate surface was polished with angle grinder, the C2 powder was mixed according to the mass percentage of pure metal powder (purity is 99.99%) as shown in Table 1. The C1 alloy powder was purchased from Sino pharm Group. Furthermore, the C2 alloy powder was weighed 200 g, then placed

Table 1 Chemical composition of NiCrSiFeBW–CeO₂ powder and Ni60 alloy powder (wt%)

Powder	Type	Ni	Fe	Cr	C	B	Si	W	CeO ₂
C1	Ni60 alloy powder	Bal	3.0	16.0	0.6	3.5	4.0	0	0
C2	NiCrSiFeBW–CeO ₂	Bal	3.0	16.0	0.6	4.5	6.0	3.0	1.0

together with the grinding balls in a ball mill jar (the mass fraction of the grinding balls was 20%), and blended for 8 h to prepare homogeneously the powder.

2.2 Laser Cladding

The FL-Dlight02-3000W semiconductor laser is used to prepare coatings. Figure 1 shows the cladding principle of the YAG laser and the 1:10 repair scale piece cladded on the 45# steel plate. Table 2 shows the process parameters of the laser deposition coating. The EAD can be obtained from the formula [19]:

$$EAD = \frac{P}{D \cdot V} \quad (1)$$

where P is the laser power (W); V is the scanning speed (mm/s); D is the laser spot diameter (mm). The scanning speed was adjusted under the condition that the other process parameters were constant, then a multi-pass lap coating (40 mm × 50 mm × 3 mm) with 6 layers was prepared.

2.3 Experimental Methods

The metallographic specimens were obtained by wire cutting the cross-section of the coatings (X–Z plane). Then the microstructure of the novel Ni-based alloy coatings was

Table 2 The composite powder and the optimized parameters

Specimens	Scanning speed (mm/s)	Spot diameter (mm)	Laser power (W)	EAD (J/mm ²)
Ni60	3	4	2000	166
1#	3	4	2000	166
2#	4	4	2000	125
3#	5	4	2000	100
4#	6	4	2000	83

characterized after etching the cross-section for 10 s in an etchant (20 mL HCl + 20 mL H₂O + 4 g CuSO₄). An optical microscope OLMPUS-GX71 (OM), Jeol-JSM-6501A scanning electron microscope (SEM), electron backscattered diffraction (EBSD), energy dispersive spectrometry (EDS), electron probe microanalysis (EPMA), PW3040/60 X-ray diffractometer (XRD, $\lambda = 0.154$ nm, 40 kV, 200 Ma Cu-K α radiation, scanning within $2\theta = 25\text{--}120^\circ$, scanning speed was 8°/min) and transmission electron microscopy (TEM) were utilized to characterize the microstructure of the coatings. The EBSD sample was polished with argon and then subjected to a second electron backscatter diffraction using Jeol-JSM-6501A. The hardness of the coatings cross-section (X–Z plane) was measured using a

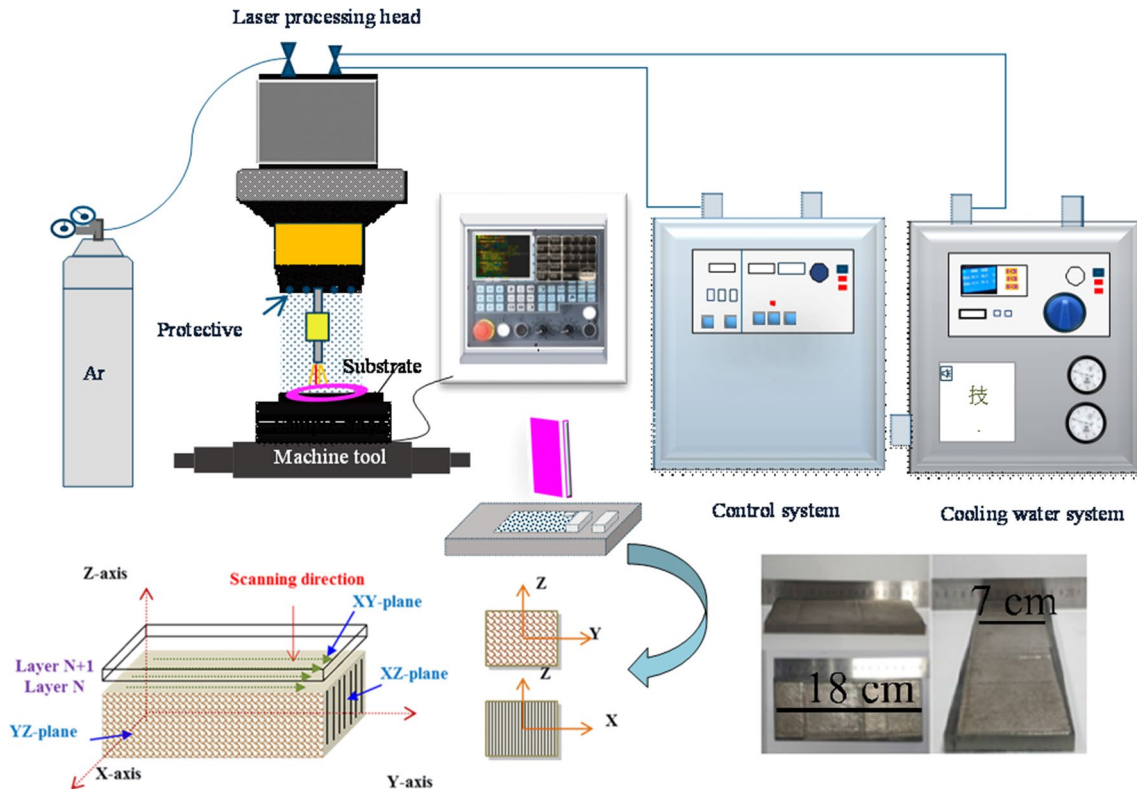


Fig. 1 Diagram of laser cladding process

WILSON-WOLPER-450SVD Vickers microhardness tester (100 N loading, 10 s load-dwell).

The abrasion resistance test was performed using friction and wear tester NANOVEA. The abrasive material was Al_2O_3 ceramic ball ($d=6$ mm, its surface hardness is higher than HRC 90 at 0–30 °C), and the size of the test sample was 10 mm \times 10 mm \times 3 mm, the load force was 10 N and the rotation speed was 200 rpm. The ceramic ball made linear reciprocating manner movement on the test samples surface during the abrade test process, which sliding distance L was 54 m. After the rubbing test, the sample was placed in an alcohol ultrasonic cleaning device for 5 min, and the specific wear rate was tested.

The CS350 type electrochemical workstation was used for electrochemical testing, and the sample dimension was 10 mm \times 10 mm \times 3 mm. Besides, the system of electrochemical workstation consisted of three parts: the reference electrode was a saturated calomel electrode (SCE), and the counter electrode was Pt. The 3.5 wt% NaCl solution was maintained at room temperature throughout the experiment, and the measurements were performed after 15 min immersions in the solution until the open circuit potential was stabilized. The corrosion characteristics of the failed metal parts are mainly the corrosion of metal by Cl^- ions during rolling. Generally speaking, the Cl^- ions concentration of industrial water is about 2000 mg/L (0.002 wt%), the higher the chloride concentration, the more serious the metal corrosion. The 3.5 wt% NaCl solution used in the experiment is a simulated seawater solution system, which is far higher than the chloride ion concentration in the working environment of the rolling mill. The experimental corrosion environment is more severe and can better meet the repair requirements. The polarization curve was obtained by a potentiodynamic sweep, the scan range and the scan rate were -0.5 to 1.0 V, 0.33 mV/s, respectively.

3 Results and Discussion

3.1 Alloy Composition Design

The T–P diagrams of two alloys during the equilibrium solidification condition calculated by using the Nickel based superalloy database module of JMatpro software are shown in Fig. 2 [20]. The hardness values of C1 and C2 simulated by using Mechanical properties module of JMatpro software are 24.2 HRC and 45.2 HRC, respectively. Figure 2a shows that the mainly phases in C1 alloy coating include γ , γ' , M_7C_3 , M_3B_2 . Among them, a large amount of precipitated M_3B_2 phase (31 wt%) is a high-temperature phase [21, 22], and its content varies greatly with temperature decrease. The content of M_3B_2 gradually decreases at the temperature interval of 820–900 °C, while stable below 820–900 °C. Figure 2b shows that the mainly phases in C2 coating involve γ' , M_7C_3 , M_3B_2 , MB_2 , M_{23}C_6 . Comparatively, the content of γ' (48 wt%) and M_3B_2 (42 wt%) in C2 coating is significantly higher than C1 alloy, while the content of M_7C_3 (4 wt%) has declined a little, besides the novel phases M_{23}C_6 (7.6 wt%) and MB_2 (1 wt%) are generated in C2 coating [23]. It was found that the content of γ phase decreased, while the content of γ' phase and high temperature borides (M_3B_2) increased with the increase of B, Si and W elements. Adding rare earth elements to the alloy coating can remove the harmful impurities, reduce the crack source and improve the comprehensive properties of the alloy. However, the addition of rare earth elements can promote the precipitation of M_{23}C_6 type carbide at the grain boundary, which is harmful to the corrosion resistance of the coating. Therefore, the addition of CeO_2 could reduce the slag in the molten pool, and the decomposition of Ce at the laser cladding process plays a role of strengthening and refining the grains.

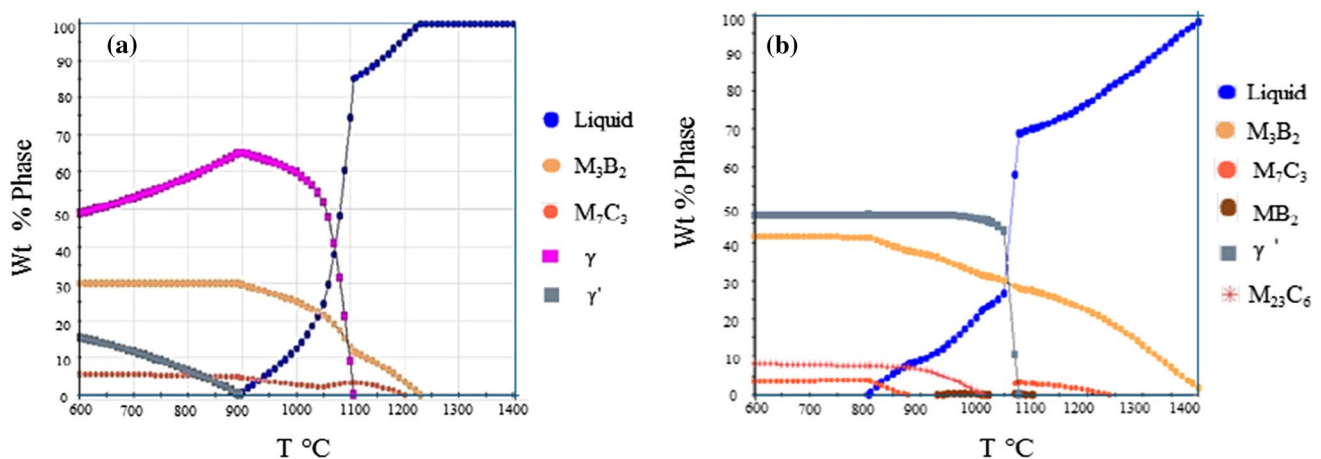


Fig. 2 Simulated temperature–phase diagram of Ni60 and NiCrSiFeBW– CeO_2 powder. a Ni60; b NiCrSiFeBW– CeO_2

3.2 Microstructural Characteristics of NiCrSiFeBW–CeO₂ Coating

Figure 3 presents the SEM morphologies of the NiCrSiFeBW–CeO₂ coatings prepared under different EAD. The microstructure of NiCrSiFeBW–CeO₂ coating (X–Z plane) is composed of columnar dendrite and equiaxed grains. It can be observed that there are two kinds of micromorphology in each coating, which are γ -Ni type phase and some precipitates. And the change of EAD has some effects on the morphology and the uniformity of the alloy coating structure. When the EAD was 166 J/mm², the elements of the NiCrSiFeBW–CeO₂ coating were sufficiently diffused during the laser cladding process because of the long heating time. However, due to the high energy, some light elements (such as B, C, etc.) were partially evaporated and lost during the cladding process, resulting in the microhardness

decrease of the NiCrSiFeBW–CeO₂ coating. The instantaneous heating temperature and heating time of the coating were correspondingly reduced as the EAD decreased. Therefore, the behavior of element diffusion in the coatings was possibly insufficient because of the low EAD so that 1#–3# coatings exhibited uniform microstructure while 4# coating was non-uniform [24].

Table 3 shows the relative atomic mass of various elements inside the columnar dendrite (point 1) and at the dendrite arm (point 2) in the 1#–4# coatings. It can be seen that the content of B and O at the dendrite arm is higher while the content of Ni (in 1#–3# coatings) and Fe is lower than that inside dendrites. Besides, the content of Ni at point 1 and point 2 is similar, because the cooling rate of 4# coating is fast when the EAD is too low (the scanning speed is too fast), and the Ni element can not fully diffuse. And EDS results show that the EAD has great influence on the content

Fig. 3 SEM morphologies of the NiCrSiFeBW–CeO₂ coatings with different EAD: **a** 1#; **b** 2#; **c** 3#; **d** 4#

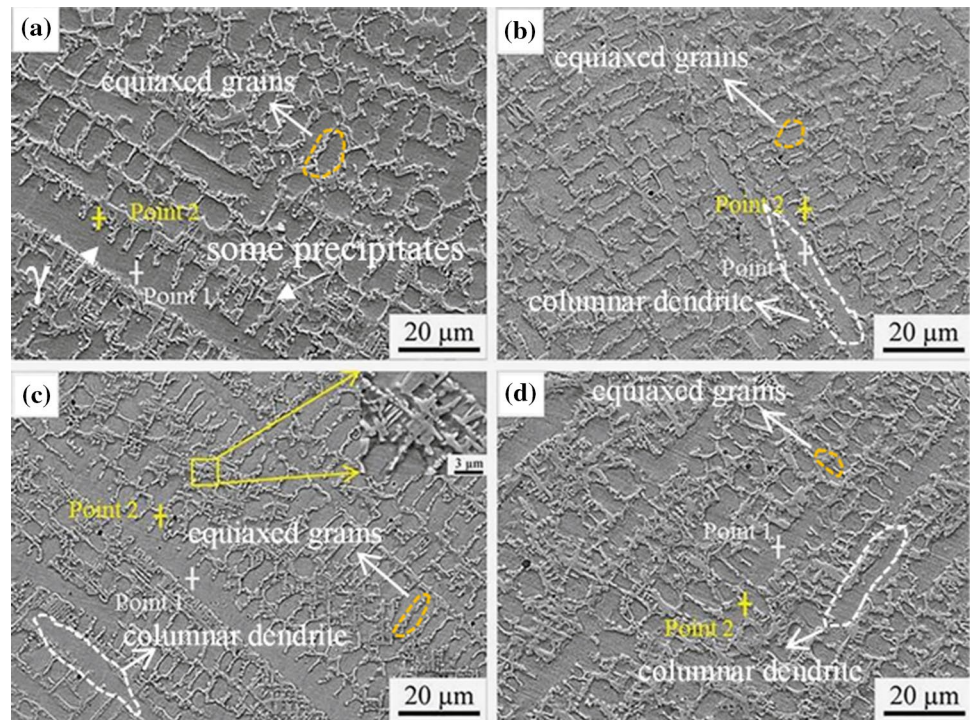


Table 3 EDS quantification analysis of locations labeled 1, 2 in Fig. 3 (at%)

	Sample	B	C	O	Si	Cr	Fe	Ni	Ce	W
Point 1	1#	5.40	13.88	0.29	6.43	13.03	10.02	50.33	0.01	0.8
	2#	3.68	12.37	0.94	8.42	10.01	9.12	55.00	0.07	0.78
	3#	2.89	12.31	0.71	6.64	14.03	9.72	52.87	0.02	0.815
	4#	13.27	30.32	0.55	4.25	9.03	8.51	33.67	0.01	0.47
Point 2	1#	9.64	11.15	5.74	20.95	1.53	1.79	49.19	0.04	1.81
	2#	15.30	31.64	1.39	5.95	6.10	5.48	34.26	0.01	3.15
	3#	12.47	21.39	3.56	13.45	3.86	3.63	41.725	0.02	0.56
	4#	19.37	16.15	1.28	3.85	16.61	7.14	34.65	0.01	1

of B, C, Cr, W, O, Si, Ni and Ce. In general, due to the high energy in the laser cladding process, most of the rare earth oxide CeO_2 added will decompose, and a small amount will remain on the grain boundary, hindering the grain growth. The C and B contents in the γ -Ni type phase dendrites decreased first and then increased as the EAD decreased, while the concentration of C in the 4# sample reached the highest. The fact is that the EAD in the 1# coating was relatively higher during laser cladding process, and the powder melting and solidification time was longer than that of the 2#–4# coatings, so the atomic diffusion in the coating was more sufficient in 1# coating. The element of C and B were dissolved in the γ -Ni matrix interstice to form the interstitial solid solution, leading to a certain degree of lattice distortion to improve the strength of coatings. The higher the concentration of solute atoms, the stronger the strengthening effect was, but which is not a linear relationship. In addition, self-interstitial atom (B, C) often preferentially distributes on dislocation lines to anchor dislocations, which further enhance alloy coating wear resistance property.

To characterize the grain size and orientation of the γ -Ni type phase in the upper deposited layer, an EBSD analysis was performed. Figure 4 displays the IPF + GB, GB maps and grain boundary angle statistics results (low-angle $< 10^\circ$; high-angle $> 10^\circ$) of γ -Ni type phase in NiCrFeWSiB– CeO_2 coatings prepared under different EAD (X–Z plane), and reveals the orientation change and crystalline size evolution of γ -Ni type phase. It can be observed from the IPF + GB pictures (Fig. 4a, d, g, j) that the γ -Ni type phase grains under different EAD are mainly columnar crystal. In general, the γ -Ni type phase with cubic crystal structure is more likely to grow in $\langle 100 \rangle$ crystallographic direction, but because the growth direction of the γ -Ni type phase grains will follow the heat flow direction and be affected by the grain orientation of the previous cladding layer during laser cladding process, the γ -Ni type phase grains of coatings as a whole has no obvious orientation characteristics, exhibiting anisotropy. In addition, the heat flow direction will change repeatedly due to the laser reciprocating scanning path. The orientation of γ -Ni type phase grains in the coating was complex and changeable, which also proved that the high nucleation rate and density in the region of high undercooling lead to the nucleation orientation exhibited anisotropy and the grains random growth.

As the EAD decreased, the average grain size of the γ -Ni type phase structure of the 1#–4# coating was 2146 m^2 , $2055 \text{ }\mu\text{m}^2$, $1543 \text{ }\mu\text{m}^2$ and $1123 \text{ }\mu\text{m}^2$, respectively. This due to the decrease of EAD will cause the supercooling of the alloy coatings to decrease during the solidification. The correspondence between the nucleation density N and the supercooling ΔT during alloy solidification process can be described and explained according to Johnson–Mell formula [25]:

$$N = B \exp \left[-\frac{1}{3} \left(\frac{16\pi\sigma^3 T_m^3}{L_m^2 \Delta T^2 kT} \right) \right] \times \exp \left(-\frac{Q}{kT} \right) \quad (2)$$

where k is Boltzmann constant, related to the shape of the nucleus, N is the nucleation density, V_g is the crystal growth rate, Q is the activation energy of the atom from the liquid phase to the solid phase, B is ratio constant. There is a significant correlation between grain size and real-time cooling rate and the number of grains per unit area increases with the increase of cooling rate [26, 27]. According to Eq. (2), the N mainly depends on supercooling (ΔT) during the coatings solidification process. The N is inversely proportional to the ΔT^2 , and the ΔT increase with the EAD decrease of the laser molten pool during laser cladding process. The higher cooling rate and the greater supercooling temperature, the finer grains will be. Shao et al. [28] reported similar results that cooling rate decreased and grain size increased with the decrease of scanning speed, and scanning speed was inversely related to cooling rate and grain size. However, the average grain size of γ -Ni type phase in 1#–4# coatings first went up and then down with the decreases of EAD, which means the grain size of γ -Ni was not only pertinent to supercooling. The smaller the grain size could increase the number of grain boundaries, raise the resistance of dislocation movement and improve the strength of the alloy coatings. Besides, the crystal boundary structure of the 1#–4# coatings had changed a lot with the EAD decrease, and the proportion of low-angle grain boundaries (red-lines) showed a trend of rising slowly at first and then decreasing sharply. When the laser energy density was high (100, 125, 166 J/mm^2), the γ -Ni type phase grain boundary types were mainly low-angle grain boundaries (50–70%) in the coating. The low-angle grain boundaries with low interfacial energy contribute to the corrosion resistance of the coating [29].

3.3 Phase Constitution of NiCrSiFeBW– CeO_2 Coating

Figure 5 shows that the phase composition in the NiCrSiFeBW– CeO_2 coating, which is composed of γ -Ni type phase, B_3Cr_5 , CrB_4 , $(\text{Cr, Ni})_3\text{C}_2$, Cr_7C_3 , $\text{W}_3\text{Cr}_{12}\text{Si}_5$ and Ni_3Si by comparing the intensity of three sharp peaks. This result is consistent with the report of Chen et al. [11], who used similar technology with a NiCrBSi coating at high speed. The high crystalline diffraction peak of the Ni is at 44.3° , while the γ -Ni type phase is at 43.8° . This is because the interstitial atoms (such as B and C) were dissolved in γ -Ni type phase during laser cladding, which made the γ -Ni type phase lattice constant larger. The diffraction peak was shifted due to that Cr, W, and Fe occupy the lattice position of Ni. It can be seen from the XRD spectra result that there are only three peaks in the 1#–2# coatings, and their mainly phase

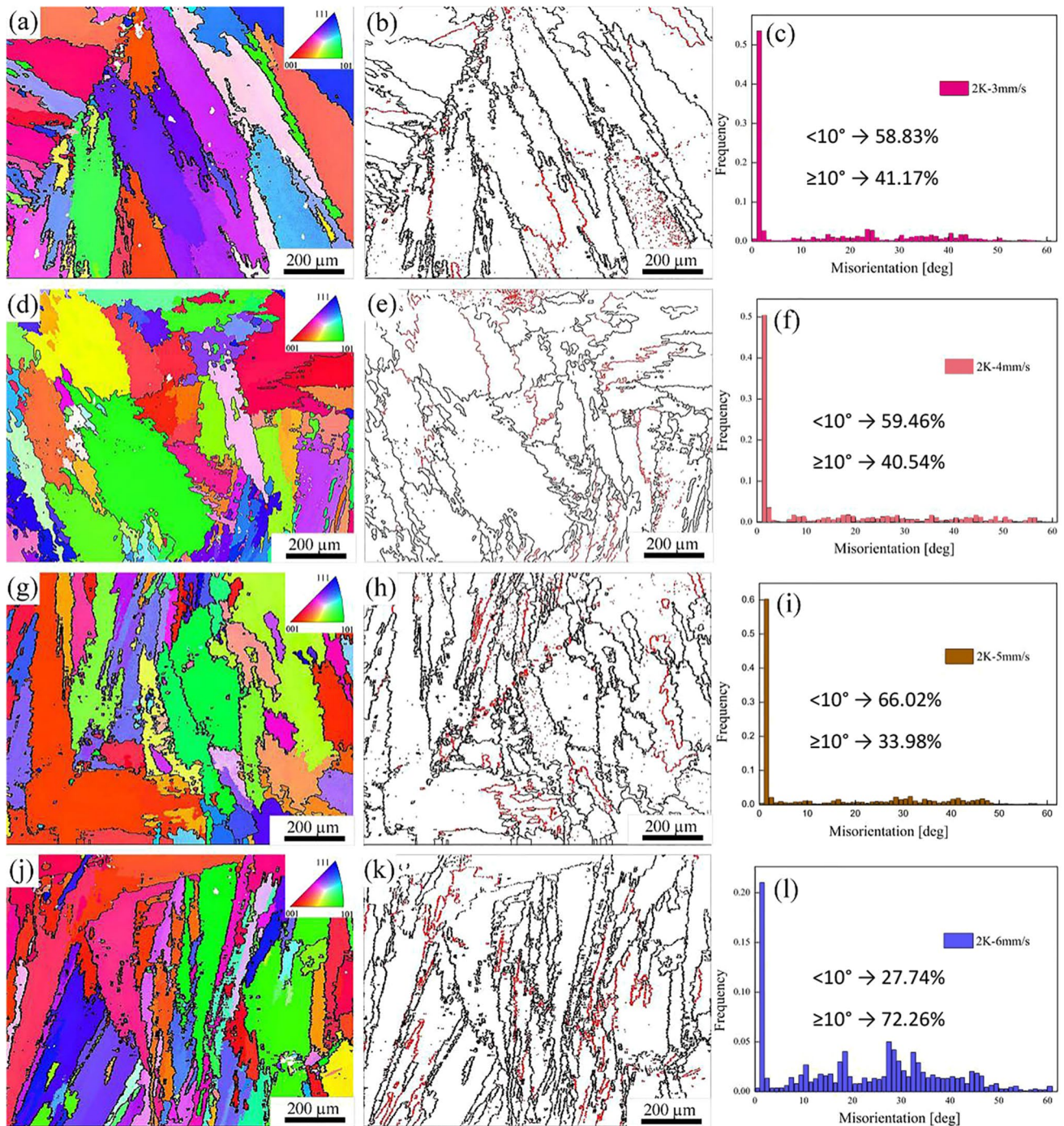


Fig. 4 The IPF+GB, GB maps and grain boundary types (low-angle $<10^\circ$; high-angle $\geq 10^\circ$) statistics graph of NiCrFeWSiB-CeO₂ coatings with different EAD: **a-c** 166 J/mm²; **d-f** 125 J/mm²; **g-i** 100 J/mm²; **j-l** 83 J/mm²

types are identified as γ -Ni type phase, W₃Cr₁₂Si₅, B₃Cr₅ and Ni₃Si.

In addition, because that the (111) crystal plane is the packed plane of FCC structure γ -Ni type phase, its intensity should be the strongest at the standard XRD pattern. Comparing the intensity and position of the diffraction peaks of

coatings 1# and 2#, it is found that the peak intensity near 51.1° increased while the peak in 43.8° intensities decreased as the energy density decreased from 166 to 125 J/mm². The reason for this change may be that the cubic structure of γ -Ni type phase in the coating was preferentially oriented in the (200) crystal face due to the decrease in energy density.

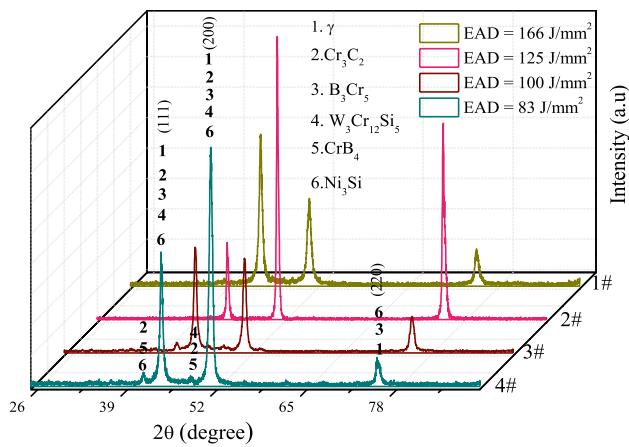


Fig. 5 XRD spectra of NiCrSiFeBW–CeO₂ coatings under different EAD

Furthermore, as the energy density continued to decrease, the XRD of 3#–4# coatings exhibited novel peak positions, which meant the generation of novel phases. The main phases in 3#–4# coatings were identified as γ -Ni type phase, B₃Cr₅, CrB₄, (Cr, Ni)₃C₂, Cr₇C₃, W₃Cr₁₂Si₅ and Ni₃Si. It can be inferred that the volume fraction of CrB₄, (Cr, Ni)₃C₂, Cr₇C₃ and Ni₃Si phases increased with the decreases of EAD, which would enhancing the wear resistance property of coatings in turn. The phases type of the thermodynamic simulation (Fig. 2b) are different from the XRD diffraction results of NiCrSiFeBW–CeO₂ coatings. It is because to that the thermodynamic simulation results were under the equilibrium solidification condition, while the laser cladding was complex non-equilibrium solidification process.

In order to further illustrate the in situ precipitation characteristics of borides, carbides and silicide in the 3# coating, EPMA spectroscopy was performed. Figure 6 shows the C and B element maps in the 3# coating. There are four types of phases, namely a fine-sized gray phase (at point 1), a white short rod-like phase (at point 2), a bulk gray phase (at point 3), and γ -Ni type phase matrix. From the surface scan of carbon (Fig. 6b), it can be seen that the bright yellow color appears at point 4, and its carbon content is higher than other locations. The difference in morphology was due to the different atomic number, which contained more heavy elements according to its lighter contrast. The distribution of the white phase and the gray phase was at the grain interface. The EPMA composition picture for C and B reveals the relatively high B concentrations in the gray phases and the higher C concentrations in the white phases. The point analysis results of EPMA represent the average elemental composition at the grain boundaries of γ -Ni flakes and unknown flakes. The quantitative analyses results reveal the mean composition of borides, carbides, silicide and the matrix as shown in Table 4. The atomic ratios of Cr to B in deep gray phase (at point 1) was 1:4, this deep block phase possibly was CrB₄. The white phase (at point 2), which was rich in C, Si, W and Cr, consisted of W₃Cr₁₂Si₅. The block gray phase with grain size 1.0–3.0 μ m (at point 3), which was rich in C, Si and Ni, consisted of Ni₃Si. Then, the gray elongated phase with the size of 1.0–1.5 μ m length and 0.4–1.0 μ m width at point 1 was regarded as CrB₄ grains. CrB₄ is a typical hard phase and is significant for the improvement of the wear resistance of the coatings [30]. Moreover, the in situ generated CrB₄ had the characteristics of strong bonding

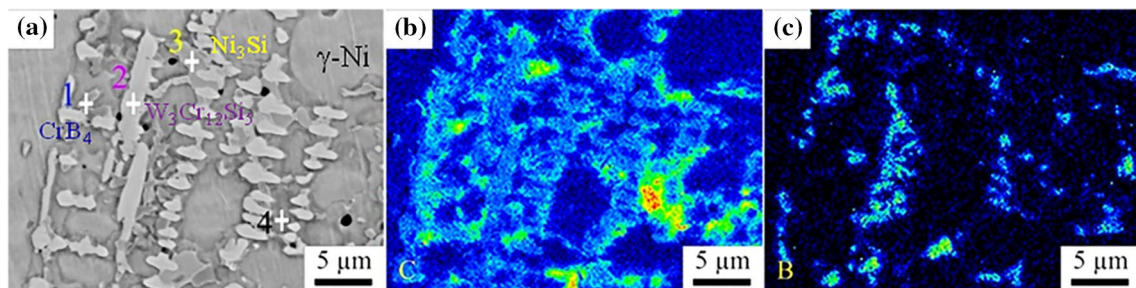


Fig. 6 The morphology and C, B elemental distribution of 3# coating: a back-scattered electron photograph, b C element distribution, c B element distribution

Table 4 The wavelength dispersive X-ray spectrometer results of point 1–4 in Fig. 6a (at%)

Point	B	C	Si	Cr	Fe	Ni	Ce	W
Point 1	51.39	9.44	3.48	12.51	2.57	20.25	0.02	0.36
Point 2	6.04	18.80	10.30	15.40	3.57	43.61	0.01	2.29
Point 3	2.25	11.34	24.24	1.70	1.18	59.29	0.01	–
Point 4	4.92	18.51	7.36	9.98	6.25	52.77	0.02	0.19

with the matrix, which the interface was clean and played a role in precipitation strengthening.

TEM was applied to further identify in situ carbide, boride and silicide particles in 3# coating. Figure 7 presents the TEM morphology (Fig. 7a) and Selected area electron diffraction pattern (SADP) of two types in situ particles, where Fig. 7b, c show the $(Cr, Ni)_3C_2$ carbides with 1 μm and Cr_7C_3 carbides with 0.5 μm ., respectively. During the solidification process, the Cr element first formed a γ -Ni substituted solid solution with Ni to improve the corrosion resistance of the matrix, and then the remaining Cr continued to react with the B and C elements at the grain boundaries to form borides and carbides. Due to the binding affinity of Cr with B stronger than that of Cr with C, Cr

preferentially combined with B to form chromium boride and then combined with C to form chromium carbide during solidification process. The borides are mainly 0.4–1.0 μm width CrB_4 (Fig. 6a) and nano- B_3Cr_5 (Fig. 8a). And $(Cr, Ni)_3C_2$ carbides are formed in the late stage of alloy coatings solidification, which will cause local segregation of Cr, and composition fluctuations near these $(Cr, Ni)_3C_2$ carbides will promote the formation of Cr_7C_3 and the two carbides maintain a specific orientation relationship [31].

Figure 8 shows the TEM morphology (Fig. 8a) and SADP pattern of the second phases. Combined with SADP and TEM-EDS result, the borides were nano- B_3Cr_5 with a tetragonal structure, which had high microhardness and stability [32]. The amount of 40 nm uniformly dispersed spherical

Fig. 7 Bright-field images and corresponding electron diffraction patterns of 3# coating: **a** the bright image of $(Cr, Ni)_3C_2$, **b** the SADP of $(Cr, Ni)_3C_2$, **c** the SADP of Cr_7C_3

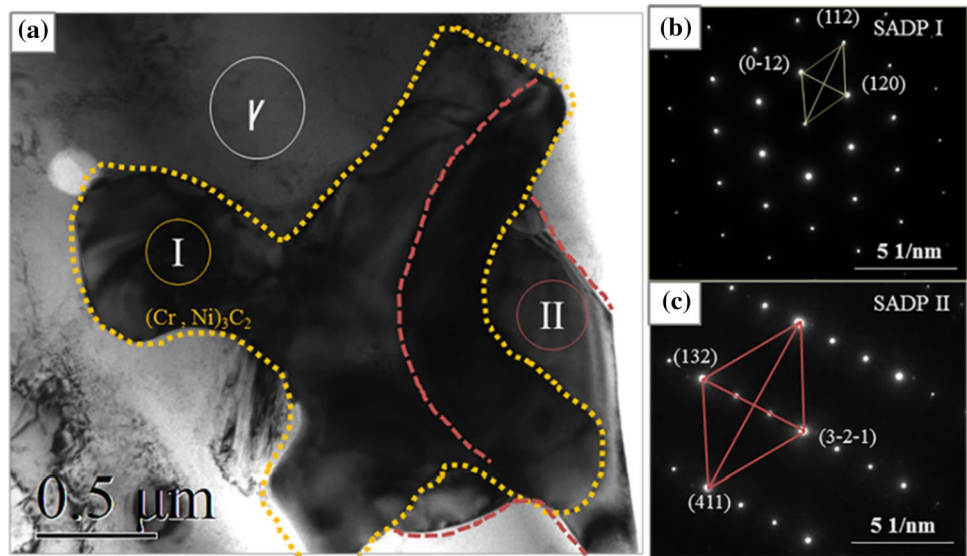
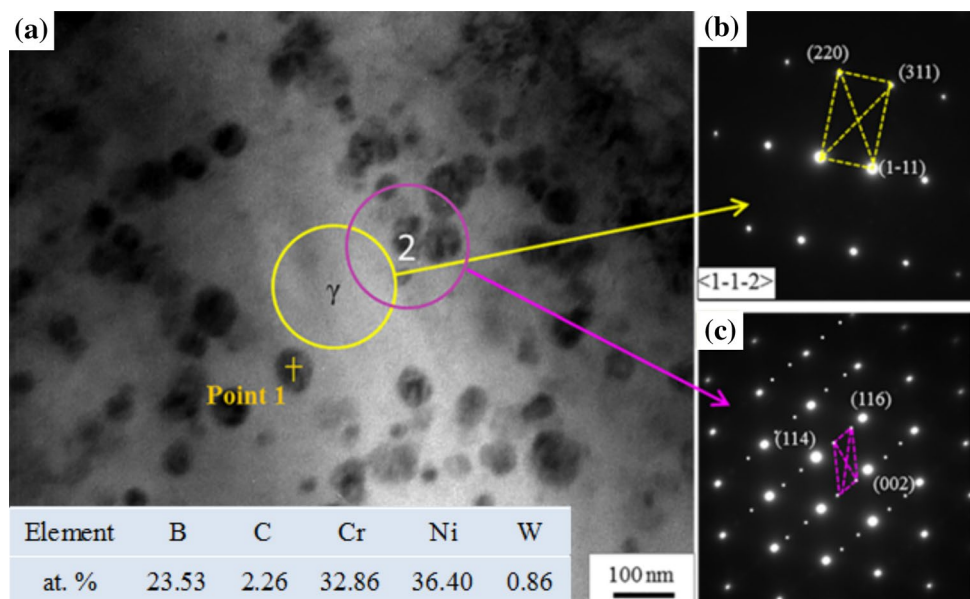


Fig. 8 Bright-field images and corresponding SADP of 3# coating: **a** the bright field image, **b** the SADP of γ -Ni, **c** the SADP of B_3Cr_5



hard nano- B_3Cr_5 particles (Fig. 8a) were inside the γ -Ni matrix in the laser cladding process, enhancing the wear resistance of the coatings. In the plastic deformation process of multiphase NiCrSiFeBW– CeO_2 coating, the nano- B_3Cr_5 particles could act as non-deformable particles and hinder the movement of dislocations. Then the strength and wear resistance of the NiCrSiFeBW– CeO_2 coating could be remarkably improved.

Figure 9 displays the TEM morphology and the elements distribution of silicide in the coating 3#. Figure 9a is two kinds of second phases are shown as white γ -Ni phase and gray silicide. From the SADP, the silicide has a hexagonal structure. And the picture of $(Fe, Ni)_5Si_3$ phase by diffraction from (100) is shown Fig. 9b. In situ-formed fishbone-like $(Fe, Ni)_5Si_3$ phase had a length of 300 nm and a width of 200 nm, which could improve the wear performance [33]. Moreover, the dispersed fish-bone $(Fe, Ni)_5Si_3$ particles were distributed in γ -Ni, forming a soft and hard phase mosaic structure with the matrix, which caused the improvement of wear resistance of the NiCrSiFeBW– CeO_2 coating.

3.4 Microhardness of the NiCrSiFeBW– CeO_2 Coating

Microhardness is one of the good indicators to reflect the wear resistance of the NiCrSiFeBW– CeO_2 coating. Figure 10 shows the average microhardness in the edge of different coatings. The hardness of the NiCrSiFeBW– CeO_2 coating obtained by the laser clad was basically consistent with the hardness of the JMatpro software simulation. The micro-hardness of 1#–4# coatings ranged from 520 to 567 $HV_{0.1}$, and the average hardness of Ni60 coating was 593 $HV_{0.1}$. Compared with the Ni60 coating, the average hardness of the novel coatings had been reduced 8%. The average microhardness of NiCrSiFeBW– CeO_2 coatings gradually increased as the EAD decrease. Firstly, one reason for 1#–4# coatings hardness increase is that the concentration of B and C elements in the γ -Ni increased as the EAD decreased, resulting in the stronger solution strengthening.

Fig. 9 TEM and TEM-EDS results of 3# specimen: **a** the bright field image and SADP of $(Fe, Ni)_5Si_3$ particle, **b** P point (100) speckle dark field image

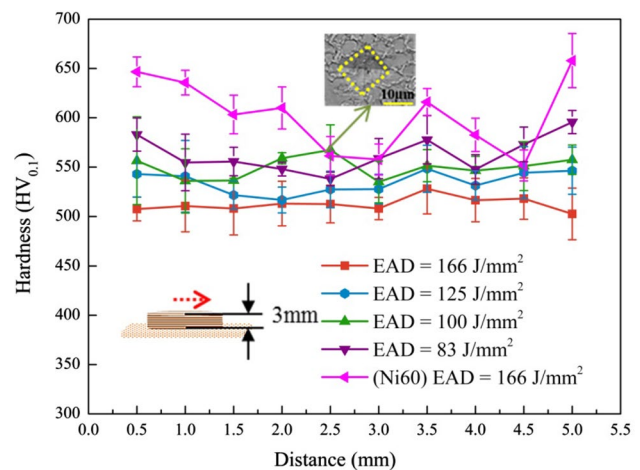
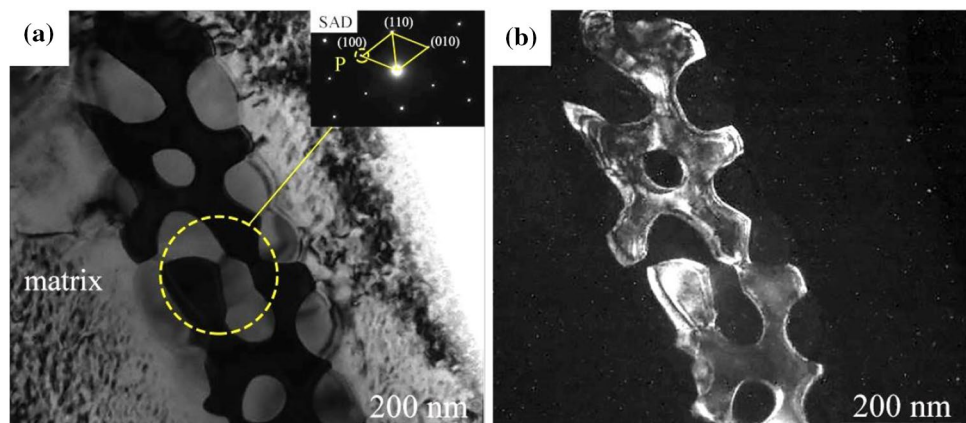


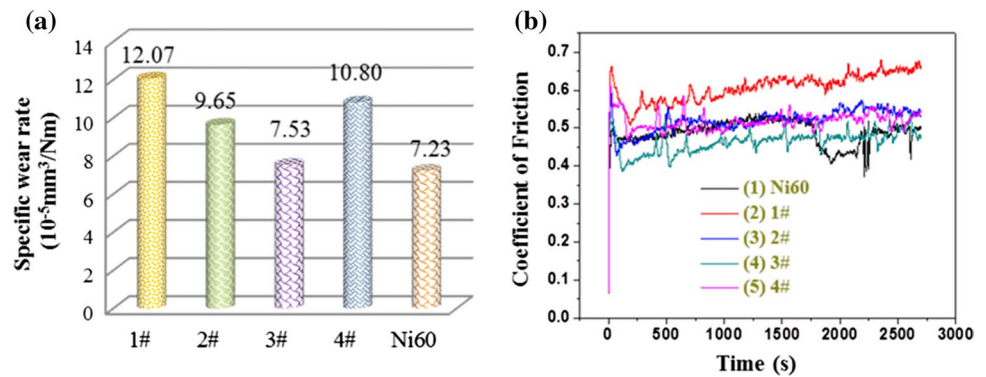
Fig. 10 Vickers microhardness of the different coatings

Secondly, the finer and denser microstructure of NiCrSiFeBW– CeO_2 coating contributing to the improvement of the hardness was formed in the cladding process [34].

3.5 Wear Resistance

The wear mass loss and the wear friction coefficient results for the 1#–4# coatings and Ni60 alloy coating were shown in Fig. 11. The variations of average coefficient of friction (COF) value reflect the lubrication effect of coatings, and the greater average coefficient of friction of coatings shows the worse lubrication effect. The COF value of 1#–4# coatings was lower at first, which was caused by the smooth of the coating surface at the beginning of wear. As the wear time increases, the COF of the coatings reached a maximum quickly and then gradually decreased and stabilizes. The COF of 1#–4# coatings reached steady at about 1750 s while Ni60 coating kept steady around 2300 s. In the meantime, during the entire wear test process, the COF values of coatings 1#, 2# and 4# were consistently higher

Fig. 11 Results of wear tests on different coatings: **a** specific wear rate of different coatings, **b** COF of different EAD



than those of 3# coating, and the friction coefficients of coatings 1#–4# showed a rising trend with increasing sliding time. After the wear test was conducted for 2700 s, the average COF values of Ni60 alloy coating and 1#–4# coatings were 0.46, 0.59, 0.51, 0.44 and 0.49, respectively. Besides, the another reason for the variation of the average COF value of 1#–4# coatings is that the increase of coatings microhardness result in the coatings smaller deformation during wear process. The wear rate of different coatings is used to evaluate wear property [35, 36]:

$$W_S = V/FL \quad (3)$$

where V is volume loss of the specimen; F is normal load and L is sliding distance. The variation in the wear rate of the 1#–4# coating is due to the fact that the material of the NiCrSiFeBW–CeO₂ coating with different microhardness surface was peeled off and the furrow was generated during the wear process, and the contact area of the Al₂O₃ ceramic ball with the sample was small so that a large amount of debris adhered to the friction surface. The change of COF value of 1#–3# coating is mainly due to the increase of hardness value of the NiCrSiFeBW–CeO₂ coating. When the hardness value of coating is relatively low (i.e. 1#, 2#), the surface scratch of coating is obvious, and the main wear mechanism of coating is abrasive wear, which causes great damage to coatings. With the increase of hardness, the wear mechanism of the coating gradually changes into adhesive wear, with some adhesive wear debris between the surfaces of the friction pairs. However, due to the poor plasticity of the 4# coating, there are a lot of adherents falling off at the abrasion peeling off place (Fig. 12d), and the surface roughness of the coating is higher than that of the 1#–3# coating in the abrasion process. The microhardness of EAD 100 J/mm² coating was 551 HV_{0.1}, and its average COF was 0.44. By contrast, the average COF value of Ni60 alloy coating were increasing to 0.46, but average wear loss mass decreased $2 \times 10^{-6} \text{mm}^3/\text{Nm}$. And 3# coating with the best wear resistance was not the highest microhardness, which indicated

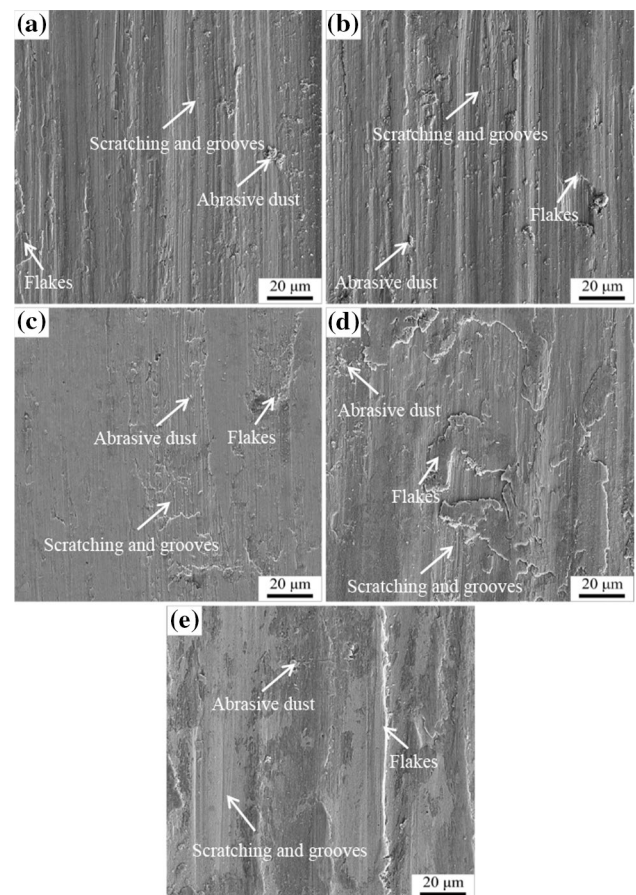


Fig. 12 SEM images of worn surfaces for different coatings: **a** 1#; **b** 2#; **c** 3#; **d** 4#; **e** Ni60

that it was not just a simple positive correlation between microhardness and wear resistance.

In order to further study the wear mechanism of the NiCrSiFeBW–CeO₂ coating and Ni60 coating, SEM was performed to analyze the worn surface characters of them. Figure 12a–d displays the worn surfaces of 1#–4# coatings. It can be seen that the wear mechanisms of the coatings were adhesive wear and abrasive wear. The scratching and grooves with different width and depth occurred in the

NiCrSiFeBW–CeO₂ coating, and the worn surface of the coatings with 100 J/mm² had the least grooves. The numbers of petal-like and strip-like W₅Cr₁₂Si₃, CrB₄, B₃Cr₅ borides and (Cr, Ni)₃C₂, Cr₇C₃ carbides in the surface of coating increased significantly with the decrease of EAD. These hard particles had a good effect on improving the anti-wear property of the coating. The higher microhardness of borides and carbides in the NiCrSiFeBW–CeO₂ coating would pin the dislocations moving at the γ-Ni matrix in the initial stage of wear. Thereby suppressing the further occurrence of plastic deformation and preventing further surface wear. In addition, the in situ hard phase particles were well bonded to the γ-Ni, which possessed a high ability to prevent plastic deformation, a large number of hard particles could be effectively supported by the γ-Ni during the abrasion process, which significantly improved the wear resistance of the NiCrSiFeBW–CeO₂ coating. Figure 12e shows the worn surfaces of Ni60 coating that the wear mechanism of Ni60 coating was abrasive wear. The plastic deformation of the wear surface was small, which was due to the higher hardness value of the Ni60 coating, but the poor plastic toughness and the surface showed obvious cutting furrow morphology [37].

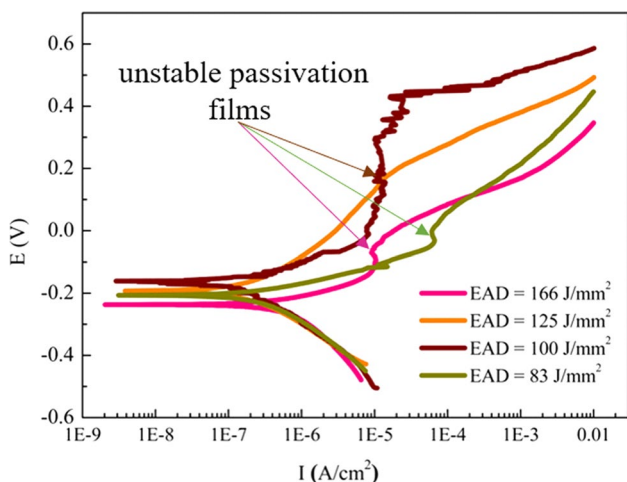


Fig. 13 Potentiodynamic polarization curves of NiCrSiFeBW–CeO₂ coatings under different EAD

3.6 Electrochemical Corrosion

Figure 13 presents cyclic potentiodynamic polarization curves of 1#–4# coatings measured in 3.5 wt% NaCl solution. The curves of the 1#–4# coatings have quite differences in shape. It can be deduced that passivation films (corrosion product film formed under neutral conditions) were formed on the surface of the 1#–4# coatings during the corrosion processes and the passivation films formed on the 1#, 2#, and 4# coatings surface were unstable. According to the lower corrosion current density which indicated a lower corrosion rate, the corrosion rate of 1#–4# coatings at first decreased and then increased [13, 38]. And the E_{corr} (Self corrosion potential), i_{corr} (Self corrosion current density), v and d from the curves were summarized in Table 5. The corrosion rate of the NiCrSiFeBW–CeO₂ coating in 3.5 wt% NaCl solution can be calculated by Faraday’s law:

$$v = \frac{M}{nF} i_{corr} = 3.73 \times 10^2 \frac{M_{Ni}}{n} i_{corr} \tag{4}$$

$$d = \frac{v}{\rho} = 3.28 \times 10^3 \frac{M_{Ni}}{n\rho} i_{corr} \tag{5}$$

where v is corrosion rate; d is corrosion deep (mm/a); F is Faraday’s constant; ρ is alloy coating density; n is atomic value of coatings (Ni), and Ni-based alloy coatings is $2e^-$, M is relative atomic mass of Ni. The as-deposited 3# sample had the highest E_{corr} (– 0.1738 V) and the lowest i_{corr} (1.88×10^{-7} A/cm²), the variation of the E_{corr} and i_{corr} for the 1#–4# coatings might be attributed to the fact of the Cr element the solid solution degree in γ-Ni matrix during laser cladding process. The solid solution of Cr element in the γ-Ni matrix could increase the electrode potential of the matrix and could easily form a protective film on the coating surface, improving the corrosion resistance of NiCrSiFeBW–CeO₂ coating.

Figure 14a–c present the surface morphologies of 2#, 3# and Ni60 alloy coatings after electrochemical corrosion test, which indicate less regions corrosion damage in 2# and 3# coatings, while large and more regions in Ni60 alloy coating. Local corrosion occurred on the surface of the NiCrSiFeBW–CeO₂ coating, while general corrosion occurred on the surface of Ni60 alloy coating. A large number of small flaky and spherical boride particles

Table 5 Comparison of self-corrosion potential of NiCrSiFeBW–CeO₂ coating

Sample	1#	2#	3#	4#	Ni60 [10]	718 [12]
E_{corr}/V	– 0.2230	– 0.2004	– 0.1738	– 0.2078	– 0.7385	– 0.3020
$i_{corr}/(A/cm^2)$	2.41×10^{-7}	2.31×10^{-7}	1.88×10^{-7}	4.05×10^{-7}	1.15×10^{-2}	3.37×10^{-5}
$v/(g/m^2h)$	2.63×10^{-3}	2.53×10^{-3}	2.06×10^{-3}	4.43×10^{-3}	1.25×10^2	3.68×10^{-1}
$d/(mm/a)$	4.77×10^{-2}	2.72×10^{-2}	2.21×10^{-2}	5.62×10^{-2}	1.35×10^3	3.97×10

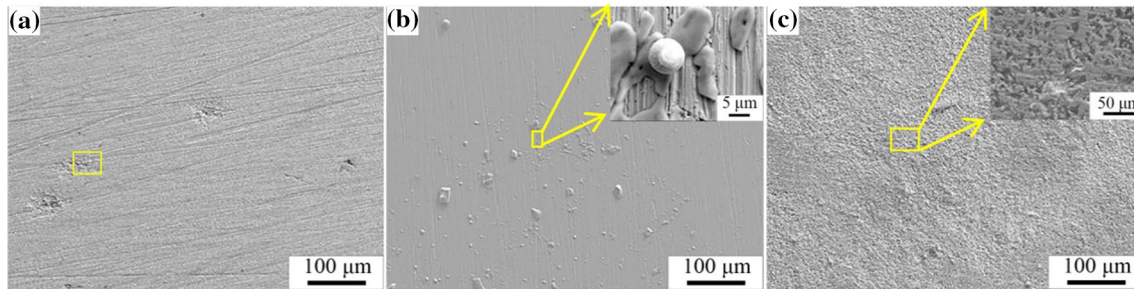


Fig. 14 SEM micrograph surface of NiCrSiFeBW–CeO₂ and Ni60 coating after electrochemical test: **a** 125 J/mm², **b** 100 J/mm², **c** Ni60–166 J/mm²

precipitated on the surface of the NiFeCrSiBW–CeO₂ alloy coating prepared under EAD of 100 J/mm², which might be increased the corrosion potential and reduce the corrosion rate of coating during the polarization process.

It can be found that the high content of Cr, Cl and O in the damaged corrosion product film in 2# coating from the Fig. 15. With the gradually increase of the electrode potential, Cl⁻ ions was easily adsorbed on the coating surface and quickly destroyed the surface passivation film due to its small atomic radius. Hence, the pitting pits are formed on the passivation film on the surface of the coating that destroyed the Cl ions in the electrochemical test. As the EAD decrease, the refinement of γ -Ni matrix delays the erosion of Cl⁻ corrosive ions, and also reduced the impurity content at the unit grain boundary and the degree of component segregation under rapid cooling conditions. Thereby reduced the effect of accelerating corrosion due to the formation of current. Meanwhile, the grain size of other components and substructures such as the precipitated phase and ordered region were reduced, which provided a reliable guarantee for improving corrosion resistance. The microstructure of NiCrSiFeBW–CeO₂ coating

became nonuniform when the laser energy was too low, resulting in the 4# coating corrosion rate increased.

4 Conclusions

1. A novel NiCrSiFeBW–CeO₂ alloy powder was designed by increasing the content of B and Si, adding tungsten and CeO₂ using JMatpro on the basis of Ni60 alloy powder composition system, and the NiCrSiFeBW–CeO₂ coating without cracks were successfully prepared by laser cladding.
2. The structures of the coatings were composed of γ -Ni solid solution phase together with 0.04–3 μ m in situ precipitation particles. In these particles, nano-B₃Cr₅, CrB₄, (Cr, Ni)₃C₂, Cr₇C₃, (Fe, Ni)₅Si₃ and W₃Cr₁₂Si₅ particles reinforced wear properties of the coatings, and nano-B₃Cr₅, W₃Cr₁₂Si₅, CrB₄ particles enhanced the corrosion resistance.
3. The laser energy density has significant effect on the microstructure and properties of the composite coating. The NiCrSiFeBW–CeO₂ coating clad by EAD 100 J/mm² had the best comprehensive properties,

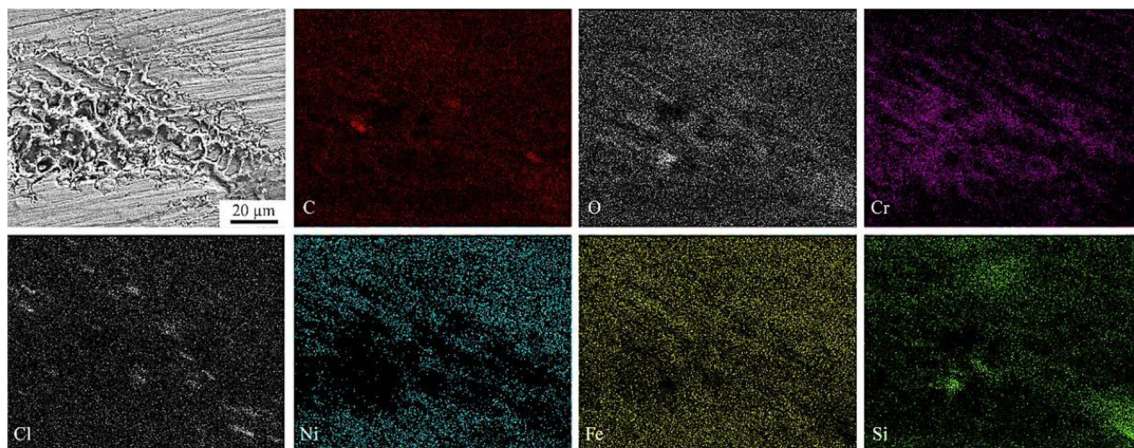


Fig. 15 SEM micrograph and elemental distribution of NiCrSiFeBW–CeO₂ coating with 125 J/mm² after electrochemical test

the hardness reached 551 HV_{0.1}, the wear loss was 7.53×10^{-5} mm³/Nm, the E_{corr} was – 0.1738 V, the i_{corr} was 1.88×10^{-7} A/cm², Compared with Ni60 alloy coating, the E_{corr} was improved by 76.4%.

4. The novel NiCrSiFeBW–CeO₂ coating not only has good laser cladding formability but also has high wear resistance and high corrosion resistance, and it can be used to repair fretting damaged metal parts of short stress wire.

Acknowledgements This work was financially supported by Green Manufacturing System Integration Project of the Industry and Information Ministry of China (2017), National Key R&D Program of China (2016YFB1100201), Research and development plan for the future emerging industries in Shenyang (18-004-2-26), and Shenyang Achievement Transformation Project (2019).

References

1. A. Chergui, K. Hadj-Hamou, F. Vignat, *Comput. Ind. Eng.* **126**, 292–301 (2018)
2. B.S. Richardson, R.F. Lind, P.D. Lloyd, M.W. Noakes, L.J. Love, B.K. Post, *Addit. Manuf.* **24**, 467–478 (2018)
3. J. Liu, H. Yu, C. Chen, F. Weng, J. Dai, *Opt. Lasers Eng.* **93**, 195–210 (2017)
4. N. Li, S. Huang, G.D. Zhang, R.Y. Qin, W. Liu, H.P. Xiong, G.Q. Shi, J. Blackburn, *J. Mater. Sci. Technol.* **35**, 242–269 (2019)
5. A. Haleem, M. Javaid, A. Saxena, *Egypt. Hear. J.* **70**, 433–441 (2018)
6. Z. Weng, A. Wang, X. Wu, Y. Wang, Z. Yang, *Surf. Coat. Technol.* **304**, 283–292 (2016)
7. S. Zhou, X. Dai, *Appl. Surf. Sci.* **256**, 4708–4714 (2010)
8. S. Sun, H. Fu, X. Ping, X. Guo, J. Lin, Y. Lei, W. Wu, J. Zhou, *Appl. Surf. Sci.* **476**, 914–927 (2019)
9. X.B. Liu, C. Zheng, Y.F. Liu, J.W. Fan, M.S. Yang, X.M. He, M. Di Wang, H.B. Yang, L.H. Qi, *J. Mater. Process. Technol.* **213**, 51–58 (2013)
10. X. Luo, J. Li, G.J. Li, *J. Alloys Compd.* **626**, 102–111 (2015)
11. X. Chen, X. Qin, Z. Zhu, K. Gao, *J. Mater. Process. Technol.* **262**, 257–268 (2018)
12. C. Wang, Y. Gao, G. Zhang, *Rare Met. Eng.* **46**, 2306–2312 (2017)
13. X. He, R.G. Song, D.J. Kong, *J. Alloys Compd.* **770**, 771–783 (2019)
14. H. Zhang, D. Gu, L. Xi, H. Zhang, M. Xia, C. Ma, *J. Mater. Sci. Technol.* **35**, 1128–1136 (2019)
15. Y. Lei, R. Sun, Y. Tang, W. Niu, *Opt. Lasers Eng.* **66**, 181–186 (2015)
16. G. Yin, S. Chen, Y. Liu, *J. Mater. Eng. Perf.* **27**, 1154–1167 (2018)
17. F. Liu, C. Liu, S. Chen, X. Tao, M. Wang, *Surf. Coat. Technol.* **201**, 6332–6339 (2007)
18. Y. Zhou, S. Chen, X. Chen, T. Cui, J. Liang, C. Liu, *Mater. Sci. Eng. A* **742**, 150–161 (2019)
19. L. Bian, S.M. Thompson, N. Shamsaei, *JOM* **67**, 629–638 (2015)
20. L. Yanan, S. Ronglu, N. Wei, Z. Tiangang, L. Yiwen, *Opt. Lasers Eng.* **120**, 84–94 (2019)
21. B.C. Yan, J. Zhang, L.H. Lou, *Mater. Sci. Eng. A* **474**, 39–47 (2008)
22. Z. Jiang, P. Wang, D. Li, Y. Li, *J. Mater. Sci. Technol.* (2019). <https://doi.org/10.1007/s40195-017-0604-5>
23. W.P. Tian, H.W. Yang, S. De Zhang, *Acta Metall. Sin. Engl. Lett.* **31**, 308–320 (2018)
24. T. Hu, Z. Shi, W. Shao, X. Xing, Y. Zhou, Q. Yang, *Surf. Coat. Technol.* **377**, 124850 (2019)
25. Z.Y. Liu, Z. Wang, *J. Mater. Sci. Technol.* **34**, 2116–2124 (2018)
26. A. Viswanathan, D. Sastikumar, H. Kumar, A.K. Nath, *Surf. Coat. Technol.* **203**, 1618–1623 (2009)
27. M.H. Farshidianfar, A. Khajepour, A.P. Gerlich, *J. Mater. Sci. Technol.* **231**, 468–478 (2016)
28. J. Shao, G. Yu, X. He, S. Li, R. Chen, Y. Zhao, *Opt. Laser Technol.* **119**, 105662 (2019)
29. T. Minoda, H. Yoshida, *Metall. Mater. Trans. A* **33**, 2891–2898 (2002)
30. H.Y. Gou, Z.P. Li, H. Niu, F.M. Gao, J.W. Zhang, R.C. Ewing, J. Lian, *Phys. Appl.* **111907**, 2–6 (2013)
31. H. Xu, W. Liu, F. Lu, P. Wang, Y. Ding, *Mater. Charact.* **130**, 270–277 (2017)
32. F. Yuan, S. Forbes, K.K. Ramachandran, Y. Mozharivskiy, *J. Alloys Compd.* **650**, 712–717 (2015)
33. H. Li, J. Jie, S. Liu, Y. Zhang, T. Li, *Mater. Sci. Eng. A* **704**, 45–56 (2017)
34. K.S. Bal, J. Dutta Majumdar, A. Roy Choudhury, *Corros. Sci.* **157**, 406–419 (2019)
35. Y. Sui, F. Yang, G. Qin, Z. Ao, Y. Liu, Y. Wang, *J. Mater. Process. Technol.* **252**, 217–224 (2018)
36. D. Deschuyteneer, F. Petit, M. Gonon, F. Cambier, *Surf. Coat. Technol.* **283**, 162–171 (2015)
37. C. Guo, J. Zhou, J. Chen, J. Zhao, Y. Yu, H. Zhou, *Wear* **270**, 492–498 (2011)
38. J. Xu, C. Zhou, S. Jiang, *Intermetallics* **18**, 1669–1675 (2010)

Publisher's Note Springer Nature remains neutral with regard to jurisdictional claims in published maps and institutional affiliations.